Influences of particle size and interface energy on the stress concentration induced by the oblate spheroidal particle and the void nucleation mechanism

Minsheng Huang, Zhenhuan Li *

Department of Mechanics, Huazhong University of Science and Technology, Wuhan 430074, PR China

Abstract

Separation of the particle–matrix interface and breakage of the second-phase particle are two main void nucleation mechanisms, which are directly associated with the stress concentration factors (SCFs) at the interface and within the particle, respectively. This work investigates the coupled effects of particle size and particle shape on these stress concentrations by solving an infinite solid containing an oblate spheroidal particle under remote stress boundary condition. The phenomenological strain plasticity theory by Fleck–Hutchinson [Fleck, N.A., Hutchinson, J.W., 1997. Strain gradient plasticity. In: Hutchinson, J.W., Wu, T.Y. (Eds.), Advance in Applied Mechanics, vol. 33. Academic Press, New York, pp. 295–361] is adopted to capture the size effect, various particle aspect ratios are considered to depict the particle shape effect and an interfacial energy concept is introduced to settle the double-traction equilibrium problem at the matrix–particle interface. By using a Ritz procedure, solutions about the stress concentrations are numerically achieved and three main results are found. First, the interfacial normal stress near the particle pole, the interfacial shear stress and the particle opening stress are dramatically elevated and their distributions are significantly modified by decrease in the particle size. Second, this particle size effect is influenced by the remote effective strain, remote stress triaxiality and the interfacial energy to different extent. Finally, the particle shape effect is coupled with this particle size effect, and the more oblate the particle is, the more significant the size effect on SCF elevation is. These findings are helpful for us to understand deeply the void nucleation mechanism at the micron scale.
© 2005 Elsevier Ltd. All rights reserved.

Keywords: Strain gradient plasticity; Size effect; Shape effect; Void nucleation; Interfacial energy

---

* Corresponding author. Tel.: +86 027 87543538; fax: +86 027 87543501.
   E-mail address: zhli68@public.wh.hb.cn (Z. Li).

1. Introduction

The embedment of the second phase elastic particle into the ductile metal matrix can greatly improve their mechanical properties such as stiffness, tensile strength and creep resistance (McDanels et al., 1985), but synchronously induce high stress concentrations both within the particle and at the particle–matrix interface, which can trigger voids to nucleate by particle cracking (Fisher and Gurland, 1981; Lloyd, 1991; Brechet et al., 1991) or particle/matrix interface debonding (Keer et al., 1973; Needleman, 1987; Manoharan and Lewandowski, 1990). Accurate determinations of SCFs within the particle and at the interface are crucial to predict void nucleation provided that critical strengths of the particle and the interface are known a priori.

During the last 30 years, many works have been performed to determine the stress distributions at the interface and within the particle (Tuba, 1966; Huang, 1972; Orr and Brown, 1974; Thomson and Hancock, 1984; Wilner, 1988, 1995; Tvergaard, 1993, 1995), which presented substantial understandings to the classical size-independent damage mechanism in metal matrix composites (MMCs), but are insufficient to capture the size effect on the mesoscopic stress field around particles at microns or submicrons scale since the matrix material was still modeled by the classic size-independent plasticity.

At the micron or submicron scale, wavelength of the inhomogeneous plastic deformation due to the dimensional and microstructural constraints is usually the same order as the material characteristic length, so the size effect on the material mechanical behavior is inherent (Arzt, 1998). In recent years, a series of typical mesoscopic mechanical experiments have been carried out to investigate this size-dependent behavior. Lloyd (1994) observed that the stiffness of SiC-reinforced aluminum is markedly increased with decreasing the particle size at the fixed particle volume fraction. Barlow and co-workers (Barlow and Liu, 1998; Shu and Barlow, 2000) further investigated the lattice rotation distribution around the tiny whisker via the TEM technique and found that lattice rotation field was much smoother than that predicted by the classical size-independent FEM, which was believed to be associated with the size effect. Many other physical experiments, such as the micro-indentation (Ma and Clark, 1995; McElhaney et al., 1998; Abu Al-Rub and Voyiadjis, 2004), the micro-twin (Fleck et al., 1994), the micro-bend (Stolken and Evans, 1998) and the thin film micro-necking (Huang and Spaepen, 2000; Espinosa et al., 2003, 2004), and numerous discrete dislocation simulations (Cleveringa et al., 1997, 1999a,b; Shu et al., 2001; Bittencourt et al., 2003; Deshpande et al., 2003; Shi et al., 2003) also confirm that the size effect inevitably emerges at the micron or submicron scale. The conventional plasticity theories are insufficient to capture this size effect, so various advanced strain gradient plasticity models have been developed in the last decade (Aifantis, 1984, 1987; Fleck and Hutchinson, 1993, 1997, 2001; Gao et al., 1999; Huang et al., 2000; Gurtin, 2000; Acharya and Bassani, 2000; Bassani, 2001; Gudmundson, 2004; Han et al., 2005a,b) and have been actively devoted to study the size-dependent response of the particle-reinforced composite (Shu and Barlow, 2000; Huang et al., 2000; Xue et al., 2002; Niordson and Tvergaard, 2001, 2002; Niordson, 2003; Bittencourt et al., 2003). Existing works on the particle size effect commonly considered the particles as perfect sphere or cylinder. However, in the engineering materials, the spheroidal particles are more ubiquitous, which bring more significant influences to the size effects due to significant strain gradients near high curvature surface of non-spherical particles (Huang and Li, 2005). In our pervious work, the particle was regarded as to be prolate. In fact, the void nucleation mechanism for the oblate spheriodal particles is different from that for the prolate ones. In addition, our early work only considered the displacement continuum condition but ignored the high-order traction equilibrium problem at the matrix/particle interface. To overcome these limitations, this work studies the size-dependent stress concentrations induced by the oblate spheroidal particle, and the interface energy concept is especially introduced to settle the high-order traction equilibrium problem. For simplicity, only the remote proportional and monotonic axisymmetric tension loading is considered, and the analysis is restricted to small strain cases.

2. Mechanical model and basic relations

2.1. Infinite representative model

To investigate the coupled effects of particle size and particle shape, an aggregate including infinite size-dependent non-linear matrix and an isolated oblate spheroidal elastic particle is considered as shown in Fig. 1. In the following text, the scripts m and p denote the matrix and the particle, respectively.

For convenience, both the Cartesian coordinate system (x_1, x_2, x_3) and the oblate spheroidal coordinates system (ζ, θ, φ) are adopted to accommodate the geometry of the oblate particle (see Fig. 1 and Appendix A-1).

In above two coordinate frames, the interface between the oblate spheroidal particle and the matrix material can be described by

$$\left(\frac{x_1}{b}\right)^2 + \left(\frac{x_2}{b}\right)^2 + \left(\frac{x_3}{a}\right)^2 = 1 \quad \text{or} \quad \zeta = \beta = \tanh^{-1}\mu = \tanh^{-1}\frac{a}{b}, \tag{1}$$

where the x_3-axis (i.e. the main tension axis) is aligned with the symmetry axis of the oblate spheroidal particle, a and b denote the lengths of semi-minor and semi-major axis of the particle. Obviously, the morphology of the particle can be fully described by half of the foci $\alpha = \sqrt{b^2 - a^2}$ and the aspect ratio $\mu = a/b$.

For the sake of simplicity, our attention is restricted to the small deformation case. Since the remote strain gradient η_{ijk}^{∞} is small enough at the infinite scale that the remote high-order stresses τ_{ijk}^{∞} can be neglected (Fleck and Hutchinson, 1993), only the axisymmetric proportional tension loadings, i.e. the non-zero remote uniform macroscopic stresses $\Sigma_{11} = \Sigma_{22} = Q$ and $\Sigma_{33} = P$ $(P > Q \geqslant 0)$, are applied as indicated in Fig. 1. These stipulations allow a generalization of Illuyshin's theorem to be enforced: proportional loading occurs at each material point within the solid and results of the deformation theory exactly coincide with the predictions of the flow theory (Fleck and Hutchinson, 1993).

2.2. Constitutive relation

Here, the multi-parameter phenomenological SG deformation theory (Fleck and Hutchinson, 1997) is adopted to model the isotropic and plastic incompressible matrix since it has an advantage for obtaining closed-form solutions to some basic problems (Fleck and Hutchinson, 2001). In the SG theory, the strain gradient tensor $\eta_{ijk} = u_{k,ij}$ can be decomposed as follows (Smyshlyaev and Fleck, 1996):
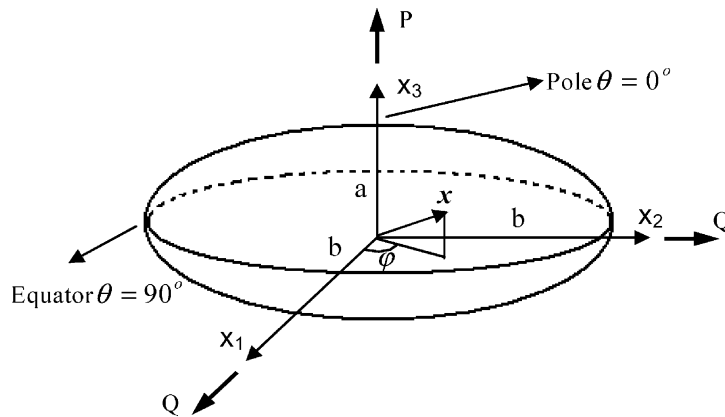

Fig. 1. Schematic showing an infinite solid containing an oblate particle, where the axisymmetric remote stress are applied as $\Sigma_{11} = \Sigma_{22} = Q$ and $\Sigma_{33} = P$ with $P \geqslant Q \geqslant 0$.

$$\eta_{ijk} = \eta_{ijk}^{H} + \eta_{ijk}^{\prime(1)} + \eta_{ijk}^{\prime(2)} + \eta_{ijk}^{\prime(3)}, \tag{2}$$

where η_{ijk}^{H} is the hydrostatic part and $\left\{\eta_{ijk}^{\prime(1)}, \eta_{ijk}^{\prime(2)}, \eta_{ijk}^{\prime(3)}\right\}$ are three orthogonal deviatoric parts.

Above decomposition provides three independent strain gradient invariants $\eta_{ijk}^{\prime(m)}\eta_{ijk}^{\prime(m)}$ ($m = 1, 2, 3$), which can be used to generalize the Von Mises effective strain ξ_e and the effective stress σ_e to include the contributions of the high-order terms as

$$\xi_e^2 = \frac{2}{3}\varepsilon_{ij}'\varepsilon_{ij}' + l_1^2\eta_{ijk}^{\prime(1)}\eta_{ijk}^{\prime(1)} + l_2^2\eta_{ijk}^{\prime(2)}\eta_{ijk}^{\prime(2)} + l_3^2\eta_{ijk}^{\prime(3)}\eta_{ijk}^{\prime(3)}, \tag{3a}$$

$$\sigma_e^2 = \frac{3}{2}\sigma_{ij}'\sigma_{ij}' + l_1^{-2}\tau_{ijk}^{\prime(1)}\tau_{ijk}^{\prime(1)} + l_2^{-2}\tau_{ijk}^{\prime(2)}\tau_{ijk}^{\prime(2)} + l_3^{-2}\tau_{ijk}^{\prime(3)}\tau_{ijk}^{\prime(3)}, \tag{3b}$$

where $\tau_{ijk}^{\prime(n)}$ are work conjugated to the deviatoric strain gradient tensor $\eta_{ijk}^{\prime(n)}$; l_1, l_2 and l_3 are three characteristic material lengths which related to the intrinsic material length l via (Begley and Hutchinson, 1998)

$$l_1 = \frac{1}{\kappa}l, \quad l_2 = \frac{1}{2}l, \quad l_3 = \sqrt{\frac{5}{24}}l. \tag{4}$$

Since $l \approx 5\ \mu m$ and $l_1 \approx 0.25\text{–}1\ \mu m$ for most metallic materials (Hutchinson, 2000), we typically set κ to 8 here.

To consider the elastic compressibility of matrix material, an elastic volume strain energy density $w_V^m(\varepsilon_V)$ is appended to the strain energy density w^m by Hwang and Huang (2002) as

$$w^m(\varepsilon, \eta) = w_V^m(\varepsilon_V) + w^m(\xi_e). \tag{5}$$

The part of $w^m(\xi_e)$ is associated with the generalized effective strain ξ_e, which can be assumed as follows:

$$w^m(\xi_e) = \frac{n}{n+1}\sigma_0\varepsilon_0\left(\frac{\xi_e}{\varepsilon_0}\right)^{\frac{n+1}{n}}, \tag{6}$$

where n is the power hardening exponent and σ_0 the reference flow stress corresponding to the reference strain ε_0.

Assuming that the matrix volume deformation is linearly elastic and the hydrostatic strain gradient η_{ijk}^{H} is so small that has no contribution to the strain energy density, the elastic volume strain energy density function can be expressed as

$$w_V^m(\varepsilon_V) = \frac{1}{2}K^m\varepsilon_V^2 \quad \varepsilon_V = \mathrm{tr}\,\varepsilon = \varepsilon_{ii}, \tag{7}$$

where $K^m = \dfrac{E^m}{3(1-2v^m)}$, E^m the Young's modulus and v^m the Poisson's ratio.

Considering σ_{ij} and τ_{ijk}' are work conjugated to ε_{ij} and η_{ijk}', respectively, σ_{ij} and τ_{ijk}' can be obtained by

$$\begin{cases} \sigma_{ij} = \dfrac{\partial w^m}{\partial \varepsilon_{ij}} = K^m\varepsilon_V\delta_{ij} + \dfrac{2}{3}\dfrac{\sigma_e}{\xi_e}\varepsilon_{ij}', \\[2mm] \tau_{ijk}'(n) = \dfrac{\partial w^m}{\partial \eta_{ijk}'} = \dfrac{\sigma_e}{\xi_e}l_n^2\eta_{ijk}^{\prime(n)} \quad \text{(the index } n \text{ no sum).} \end{cases} \tag{8}$$

On the other hand, since the particle can be assumed as an isotropic elastic solid with Young's modulus E^p and Poisson's ratio v^p, its stress–strain relation can be simply described as

$$\sigma_{ij}^p = \lambda^p\varepsilon_{kk}^p\delta_{ij} + 2G^p\varepsilon_{ij}^p, \tag{9}$$

where $\lambda^p = \dfrac{E^p v^p}{2(1+v^p)(1-2v^p)}$ and $G^p = \dfrac{E^p}{2(1+v^p)}$.

2.3. Interface energy and boundary conditions

Since the second-phase particle is elastic, the particle/matrix interface should be double-stress traction free. However, in the SG matrix side, the double-stress traction associated with the high-order stress τ_{ijk} is inevitably developed. How to settle this contradiction is mechanically important. Physically, due to the obstruction of the elastic particle, enormous dislocations developed in the matrix material can not pass the interface and inevitably accumulated at the matrix/particle interface. Hence, a dislocation layer surrounding the particle comes into being. This is likely to influence the energetic state near the interface (Cermelli and Gurtin, 2002; Gudmundson, 2004; Aifantis and Willis, 2005). Referring to Gudmundson's work (2004), an additional contribution associated with the interface energy to the internal virtual work of the SG matrix is appended as

$$\delta w_{\text{in}} = \int_{V_m} \left(\sigma_{ij} \delta \varepsilon_{ij} + \tau_{ijk} \delta \eta_{ijk} \right) \mathrm{d}V + \int_{S_p} R^I_{kj} \delta u_{k,j} \, \mathrm{d}S, \tag{10}$$

where S_p denotes the surface of the particle and R^I_{kj} is work conjugate to the displacement gradient $u_{k,j}$ at the interface of the matrix side.

As mentioned above, the remote high-order stress τ^∞_{ijk} is small enough to be neglected, and the matrix/elastic particle interface is double-stress traction free. Hence, the external virtual work of the matrix material can be expressed as

$$\delta w_{\text{ex}} = \int_{S_p} T^p_k \delta u_k \, \mathrm{d}S + \int_{S_r} T^r_k \delta u_k \, \mathrm{d}S, \tag{11}$$

where T^p_k and T^r_k are the surface tractions at the particle interface S_p and at the infinite solid surface S_r, respectively.

Applying the divergence theorem to (10) and noting the equality between the internal virtual work δw_{in} and the external virtual work δw_{ex}, we can obtain the equilibrium equation:

$$\sigma_{ik,i} - \tau_{ijk,ij} = 0 \tag{12}$$

and the boundary conditions:

$$\begin{cases} n_j R^I_{kj} + n_i n_j \tau_{ijk} = 0, \\ T^p_k = n_i(\sigma_{ik} - \tau_{ijk,j}) - D_j(n_i \tau_{ijk} + R^I_{kj}), \end{cases} \quad \text{at } S_p \tag{13a}$$

and

$$T^r_k = n_i \Sigma_{ik} \quad \text{at } S_r, \tag{13b}$$

where $D_j = (\delta_{jk} - n_j n_k) \partial_k$ is the surface-gradient operator.

Obviously, the double-stress traction $r_k = n_i n_j \tau_{ijk}$ at the interface of the matrix side is automatically balanced with $n_j R^I_{jk}$ induced by the interfacial energy.

Referring to Gudmundson's work (2004), R^I_{kj} may be directly determined from the interfacial energy density w^I via

$$R^I_{kj} = \frac{\partial w^I}{\partial u_{k,j}}. \tag{14}$$

Here, a simple isotropic w^I for the elastic/plastic interface is suggested as

$$w^I(u_{k,j}) = G_m l_I u_{k,j} u_{k,j} \quad \text{and then} \quad R^I_{kj} = \frac{\partial w^I}{\partial u_{k,j}} = 2 G_m l_I u_{k,j}, \tag{15}$$

where G_m denotes the shear modulus of the matrix and l_I is the characteristic length associated with the interface energy, which can be regarded as the effective thickness of the geometrically necessary dislocation layer surrounding the particle. If the width of a single dislocation is about 0.25 nm, the thickness of the geometrically necessary dislocation layer containing averagely 100–400 dislocations can be taken as 0.025–0.1 μm (Nicola et al., 2003). As a qualitative analysis but no loss of generality, here the interfacial characteristic length l_I is tentatively set as $l_I = 0.05$ μm.

Besides, the displacement field should be continuous across the particle/matrix interface, so

$$u^p = u^m \quad \text{on } \zeta = \beta, \tag{16}$$

where u^p and u^m denote the displacement fields within the particle and in the matrix, respectively.

2.4. Stress concentration factors

To investigate the void nucleation mechanism, three kinds of stress concentration factors (SCF), i.e. the interfacial normal SCF K_I^n, the interfacial shear stress SCF K_I^s and the particle opening SCF K_p are considered. Obviously, K_I^n and K_I^s are associated with the interface debonding mechanism; while K_p is related to the particle breakage mechanism.

As a measurement of the normal stress at the particle–matrix interface, K_I^n is introduced as

$$K_I^n = \sigma_{\varsigma\varsigma}/P \quad \text{at } \zeta = \beta \tag{17}$$

and the interfacial shear SCF K_I^s is similarly defined as

$$K_I^s = |\sigma_{\zeta\theta}|/P \quad \text{at } \zeta = \beta, \tag{18}$$

where $\sigma_{\varsigma\varsigma}$ and $\sigma_{\zeta\theta}$ are the interfacial normal stress and shear stress, respectively, which can be obtained from the solution for the stress field within the particle readily.

The particle opening SCF K_p is given by

$$K_p = \sigma_{\theta\theta}/P \quad \text{at } \theta = \pi/2, \ \zeta \leqslant \beta \tag{19}$$

in which $\sigma_{\theta\theta}$ is the opening stress on the particle equator plane.

2.5. Dimensionless characteristic length ratio

To describe the size effect on these SCFs, the radius of an "equivalent sphere particle" with the same volume as the oblate spheroidal particle is defined as the "particle equivalent radius" $r = \sqrt[3]{ab^2}$, and then two characteristic length ratios $\{\lambda_p, \lambda_I\}$ can be introduced as

$$\lambda_p = l/r = l/\sqrt[3]{ab^2} \tag{20}$$

and

$$\lambda_I = l_I/\sqrt[3]{ab^2}. \tag{21}$$

Obviously, r characterizes the geometrical scale of the particle; while l and l_I denote the physical intrinsic lengths associated with the matrix material and the interface energy, respectively.

3. Basic fields and numerical procedure

Following Lee and Mear (1999), a Ritz procedure based upon Hill's (1956) minimum principle (Budiansky et al., 1982) is here employed. As well known, rational representations for the displacement fields within

the interior particle and the exterior matrix are crucial for success of this method. Therefore, the axisymmetric displacement representations for the elastic problem (i.e. elastic particle embedded in the elastic matrix) are first developed (see Appendix A), and then they are used as a reference to construct the trail displacement fields for the elastic particle–plastic matrix problems.

3.1. Trial displacement field

For the present model, the representation developed in the appendix (A.8) can be used to describe the displacement field within the elastic particle u^p:

$$
\begin{cases}
u_\eta^p = \dfrac{\alpha^2}{h} \displaystyle\sum_{n=1,3,5,\ldots} i^{n+1} \{[H_n P_{n+1}^1(i\sinh\zeta) + (n+1)(n+\gamma_p)I_n P_{n-1}^1(i\sinh\zeta)]P_{n+1}(\cos\theta) \\
\qquad\qquad + n(n+1-\gamma_p)I_n P_{n+1}^1(i\sinh\zeta)P_{n-1}(\cos\theta)\}, \\[2ex]
u_\theta^p = \dfrac{\alpha^2}{h} \displaystyle\sum_{n=1,3,5,\ldots} i^{n+1} \{[H_n P_{n+1}(i\sinh\zeta) + n(n+1-\gamma_p)I_n P_{n-1}(i\sinh\zeta)]P_{n+1}^1(\cos\theta) \\
\qquad\qquad + (n+1)(n+\gamma_p)I_n P_{n+1}(i\sinh\zeta)P_{n-1}^1(\cos\theta)\},
\end{cases}
\tag{22}
$$

where $\gamma_p = 4(1-\nu^p)$, $h = \alpha\sqrt{\cosh^2\zeta - \sin^2\theta}$ and $\{H_n, I_n\}$ are real constants. It can be verified easily that this displacement field has proper symmetry with respect to the median plane $\theta = \pi/2$.

Following Budiansky et al. (1982) and Lee and Mear (1999), the local displacement and strain fields in the plastic matrix can be constructed as

$$
\boldsymbol{u} = \boldsymbol{U^0} + \tilde{\boldsymbol{u}} \quad \text{and} \quad \boldsymbol{\varepsilon} = \boldsymbol{E^0} + \tilde{\boldsymbol{\varepsilon}},
\tag{23}
$$

where $\boldsymbol{U^0}$ and $\boldsymbol{E^0}$ are the linear displacement field and the uniform strain field associated with the remote stress Σ_{ij} in the absence of particle. Correspondingly, the strain gradient $\boldsymbol{\eta}$ can also be written as

$$
\boldsymbol{\eta} = \boldsymbol{\eta^0} + \tilde{\boldsymbol{\eta}}.
\tag{24}
$$

Similarly, $\boldsymbol{\eta^0}$ denotes the strain gradient in the absence of particle. Since $\boldsymbol{E^0}$ is uniform, $\boldsymbol{\eta^0}$ naturally equals to zero. $\tilde{\boldsymbol{\varepsilon}}$ and $\tilde{\boldsymbol{\eta}}$ are the reduced strain and strain gradient fields associated with the reduced displacement $\tilde{\boldsymbol{u}}$, respectively.

For the axisymmetric load considered in Fig. 1, the non-zero physical components of $\boldsymbol{U^0}$ in the oblate spheroidal coordinate system can be expressed as

$$
\begin{cases}
U_\zeta^0 = \dfrac{\alpha^2}{3h} P_2^1(\cosh\zeta)(E_m^0 + E_e^0 P_2(\cos\theta)), \\[2ex]
U_\theta^0 = \dfrac{\alpha^2}{3h} P_2^1(\cos\theta)[E_e^0 - E_m^0 + E_e^0 P_2(\sinh\zeta)],
\end{cases}
\tag{25}
$$

where $E_m^0 = \frac{1-2\nu}{3E^m}(P+2Q)$ is the remote mean strain and $E_e^0 = \varepsilon_0\left(\frac{P-Q}{\sigma_0}\right)^n$ the remote effective strain.

Referring to the elastic matrix displacement field (A.8), the reduced displacement field in the non-linear matrix can be constructed in terms of a complete set of orthogonal functions as (Lee and Mear, 1999)

$$
\begin{cases}
\tilde{u}_\zeta = \dfrac{\alpha^2}{h} \displaystyle\sum_{k=0,2,4,\ldots} F_k(\zeta)P_k(\cos\theta), \\[2ex]
\tilde{u}_\theta = \dfrac{\alpha^2}{h} \displaystyle\sum_{k=2,4,\ldots} G_k(\zeta)P_k^1(\cos\theta)
\end{cases}
\tag{26a}
$$

in which the functions F_k and G_k only depend on ζ:

$$\begin{cases} F_k(\zeta) = \sum_{m=0,1,2,\ldots} i^{m+1} A_{km} Q_m^1(i\sinh\zeta), \\ G_k(\zeta) = \sum_{m=0,1,2,\ldots} i^{m+1} B_{km} Q_m(i\sinh\zeta), \end{cases}$$ (26b)

where A_{km} and B_{km} are unknown real coefficients. Obviously, the trial field (26) also has proper symmetry with respect to the median plane $\theta = \frac{\pi}{2}$.

Considering the matrix/particle interface displacement continuous condition (16), the correlation between the constants $\{H_j, I_j\}$ associated with the particle displacement field and the real coefficients $\{A_{km}, B_{km}\}$ involved in the reduced matrix displacement field is established (see Appendix B). Hence, only unknown parameters $\{A_{km}, B_{km}\}$ are independent.

3.2. Minimum functional and numerical method

According to the generalized Hill's minimums principle (1956), the actual displacement field should minimize the functional $F(\boldsymbol{u}^p, \boldsymbol{u})$:

$$F(\boldsymbol{u}^p, \boldsymbol{u}) = F^p + F^m + F^I,$$ (27)

where $\{F^p, F^m\}$ are the strain energies of the elastic particle and the non-linear matrix, respectively, and F^I is the additional interface energy for the particle/matrix interface, i.e.

$$\begin{cases} F^p = \int_{V_p} w^p(\boldsymbol{\varepsilon}^p)\,\mathrm{d}V = \int_{V_p} \left[\frac{\lambda^p}{2} \varepsilon_V^p \varepsilon_V^p + G^p \boldsymbol{\varepsilon}^p : \boldsymbol{\varepsilon}^p \right] \mathrm{d}V, \\ F^m = \int_{V_m} \left[w^m(\boldsymbol{\varepsilon}, \boldsymbol{\eta}) - w^m(\boldsymbol{E}^0, 0) - \boldsymbol{\Sigma} : \tilde{\boldsymbol{\varepsilon}} \right] \mathrm{d}V + \int_{S_p} \tilde{\boldsymbol{u}} \cdot \boldsymbol{\Sigma} \cdot \boldsymbol{n}\,\mathrm{d}S, \\ F^I = \int_{S_p} w^I(u_{i,j})\,\mathrm{d}S = \int_{S_p} G_m l_I u_{i,j} u_{i,j}\,\mathrm{d}S, \end{cases}$$ (28)

where V_m and V_p denote the volume occupied by the matrix and by the particle, respectively.

Once the functional (27) has been minimized with respect to the coefficients $\{A_{km}, B_{km}\}$ by a Ritz procedure, the deformation fields within the particle and the matrix are synchronously established.

Similar to Lee and Mear's numerical strategy (1999), the double series of the trial field (26) are truncated and thus only finite terms corresponding to $k = 0, 2, 4, \ldots, 2K$ and $m = 1, 2, \ldots, M$ remain. When this is done, the particle displacement field has simultaneously been truncated and only the terms associated with $n = 1, 3, 5, \ldots, 2K - 1$ is left. Obviously, the accuracy of this strategy lies mainly on the parameters K and M selected. To ensure the precision of the results, $K = M = 10$ are chosen here and a descent Newton–Raphson procedure is adopted to avoid numerical divergence. Fig. 2 compares the present results with the FE results by MSC-MARC® for the classical scale-independent cases. It is clear at a glance that these results have excellent agreements. This validates powerfully the representative displacement fields within the particle and in the matrix to be rational.

4. Results for the stress concentration factors

The present paper aims at studying the combined effects of particle shape and particle size on the mesoscopic stress field, so a wide range of the particle aspect ratios $\mu = \left\{ 0.999, \frac{1}{2}, \frac{2}{5}, \frac{1}{3}, \frac{1}{4} \right\}$, two particle scale length ratios $\lambda_p = \{0, 1\}$ and two corresponding interfacial characteristic length ratios $\lambda_I = \{0, 0.01\}$ are considered for several stress triaxialities $R_\sigma = \{1/3, 1, 2, 3\}$. Although more fruits can also be achieved by
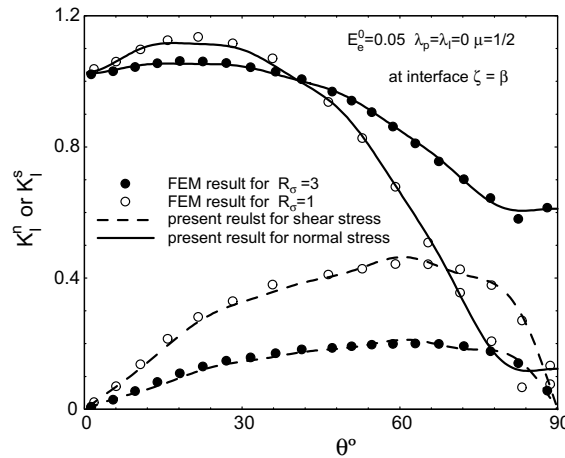
Fig. 2. The present size-independent results of the normal SCF K_I^n and shear SCF K_I^s along the matrix–particle interface in comparison with the FEM results solved by MSC-MARC® for stress triaxialities $R_\sigma = \{1,3\}$.

the present method, only the results for Poisson ratios $v^m = v^p = 0.33$ and the Young's modulus ratios $E^p/E^m = 2$ are presented here for the paper length limitation.

4.1. Influences of the interfacial energy on SCFs

To model the geometrically necessary dislocation accumulation at the interface, an interfacial energy is introduced in the present paper. As considered in (15), the interfacial energy is associated with the effective thickness l_I of the geometrically necessary dislocation layer surrounding the particle. Fig. 3 compares the influences of the dimensionless length ratio $\lambda_I = l_I/r$ on SCFs both at the interface and within the particle. For comparison, the results for the prolate spheroidal particle are also given together. It is shown in Fig. 3a that the interface energy only has very weak influence on the interfacial normal SCF K_I^n except for that near the pole ($\theta \to 0°$) of the prolate spheroidal particle, which is decreased by the interface energy to a certain extent. However, Fig. 3b indicates that the interfacial shear SCF K_I^s is clearly elevated by the interface energy both for the prolate particle and for the oblate particle. Moreover, Fig. 3c demonstrates that the maximum particle opening SCF $K_p^{o\,\max}$ is also enhanced by the interface energy especially at higher remote strain level E_e^0. In a word, for the oblate particles, the interface energy has weaker effects on the interfacial SCFs (K_I^n and K_I^s) but markedly elevates the opening SCF within the particle; while for the prolate particles, the interface energy decreases the interfacial normal SCF to a certain extent but elevates the interfacial shear and the particle opening SCFs evidently.

4.2. Interfacial stress concentration factors

The normal stress at the particle–matrix interface plays a very important role in interface debonding. Fig. 4 displays the distributions of normal SCF K_I^n along the interface, where the physical angle θ is defined as $\theta = \arctan(\mu\sqrt{x_1^2 + x_2^2}/x_3)\big|_{\zeta=\beta}$ with $\theta = 0$ and $\theta = \frac{\pi}{2}$ corresponding to the pole and equator of the particle (see Fig. 1), respectively. It can be seen that, for the classical size-independent cases (i.e. $\lambda_I = \lambda_p = 0$), the location of the maximum interfacial normal SCF $K_I^{n\,\max}$ always deviates slightly from the pole and is within the range $0 < \theta < 30°$. However, with decreasing of the particle size, the magnitudes and distributions of K_I^n
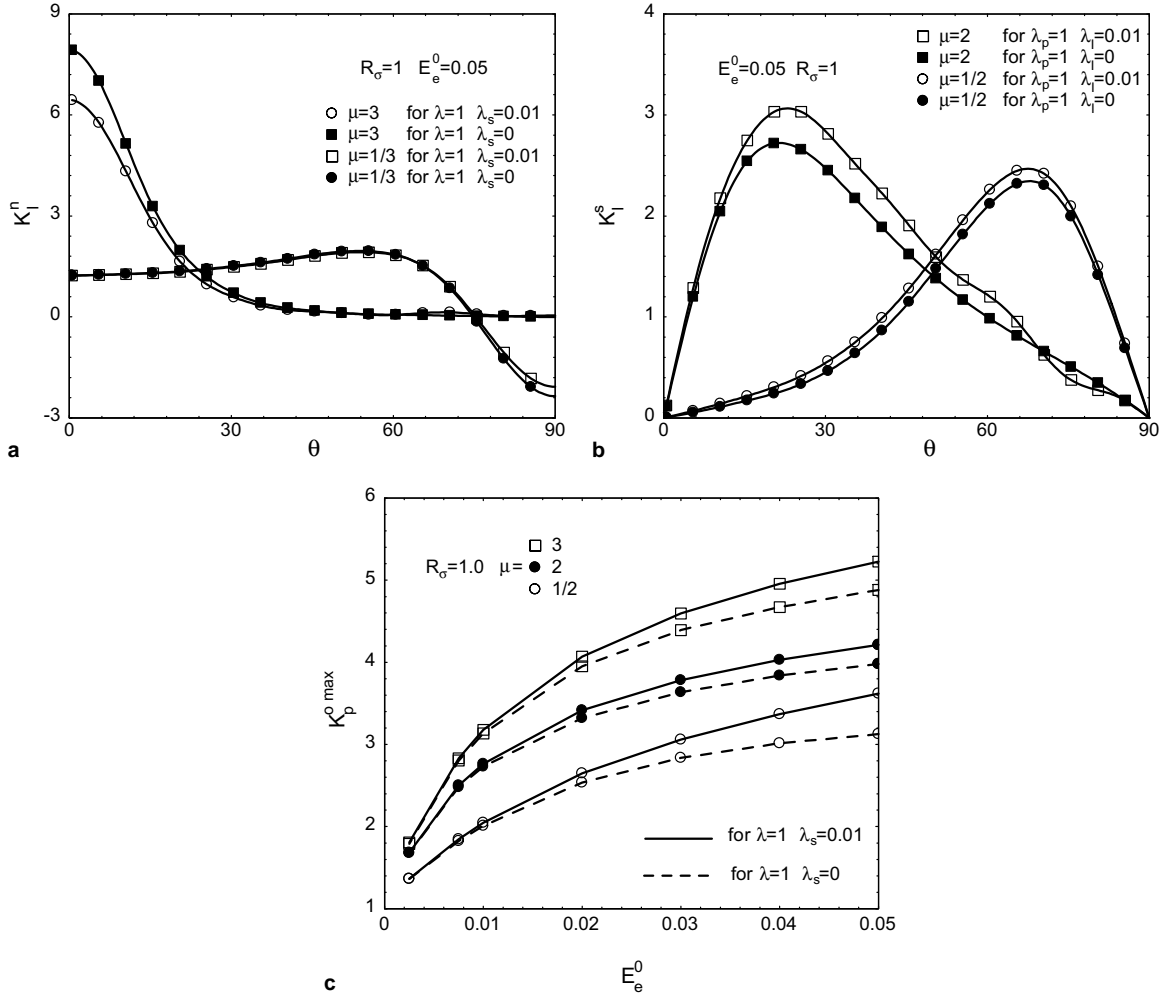
Fig. 3. Influences of the interface energy (a) on the interfacial normal SCF K_I^n; (b) on the interfacial shear SCF K_I^s and (c) on the maximum of particle opening SCF $K_p^{o\,max}$.

at the interface are dramatically modified. The interfacial normal SCF K_I^n around the poles is significantly elevated but that near the equator is heavily depressed (even to values less than zero). As a result, the maximum of SCF $K_I^{n\,max}$ is simultaneously enhanced and the location of $K_I^{n\,max}$ shifts to a place with larger angle θ. This means that the particle size effect is likely to not only advance the void nucleation initiation but also change the location of void nucleation. This finding is qualitatively consistent with Niordson's (2003) size-dependent FE results for the whisker-reinforced composite, where they reported that the normal stresses along the fiber top close to the fiber corner are significantly enhanced by the strain gradient effects.

To depict more clearly the size effect on the interfacial normal stress concentration factor, normalizing the scale dependent $\left(K_I^{n\,max}\right)^{\lambda_p=1,\lambda_I=0.01}$ by the scale independent $\left(K_I^{n\,max}\right)^{\lambda_p=\lambda_I=0}$ renders a new parameter as

$$B_I^n = \left(K_I^{n\,max}\right)^{\lambda_p=1,\lambda_I=0.01} \Big/ \left(K_I^{n\,max}\right)^{\lambda_p=\lambda_I=0}. \tag{29}$$
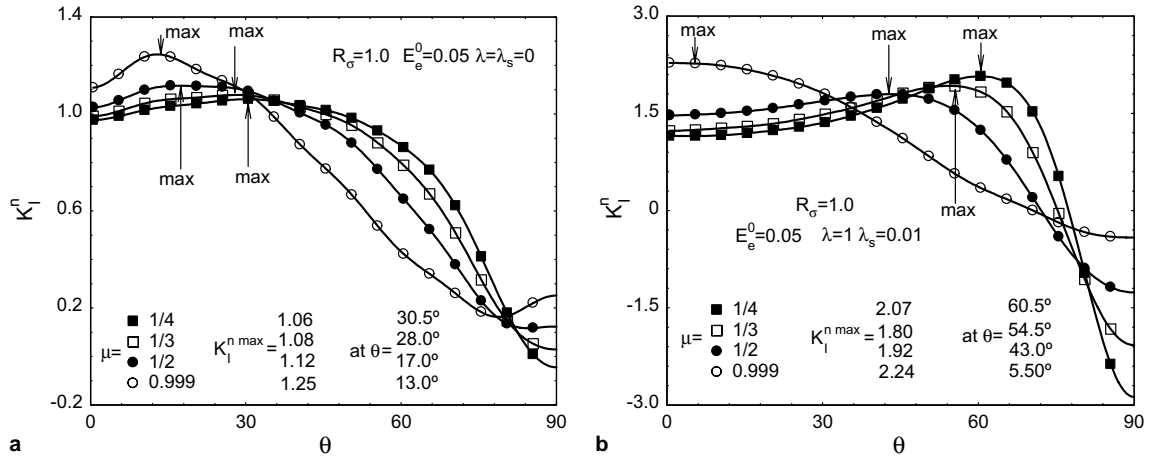
Fig. 4. Distribution of the interfacial normal SCF K_I^n along the particle surface for (a) scale-independent cases $\lambda_p = \lambda_I = 0$; (b) scale-dependent cases $\lambda_p = 1$, $\lambda_I = 0.01$.
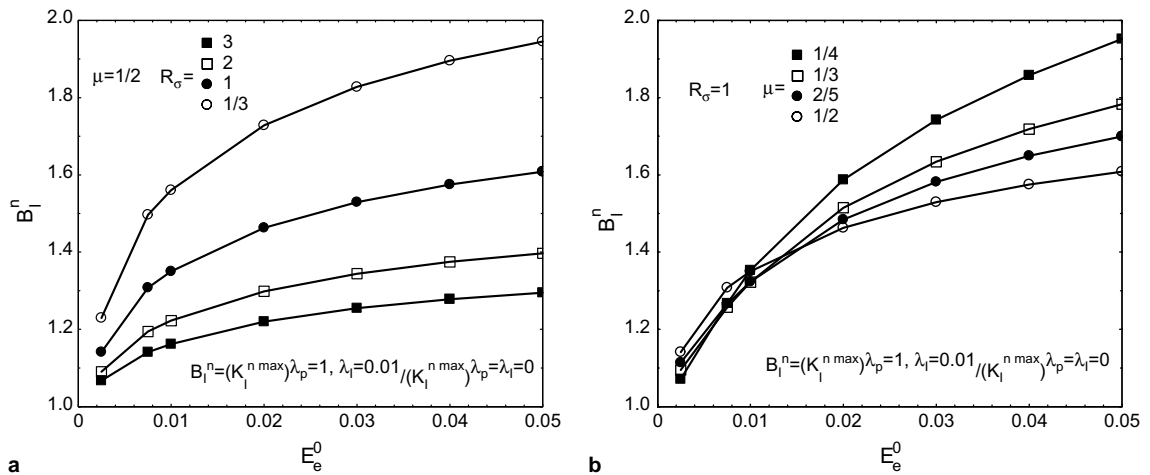

Fig. 5. Variations of B_I^n as a function of the remote effective strain E_e^0 (a) for different stress triaxialities $R_\sigma = \{1/3, 1, 2, 3\}$; (b) for particles with different aspect ratios $\mu = \{\frac{1}{2}, \frac{2}{5}, \frac{1}{3}, \frac{1}{4}\}$.

Fig. 5 illustrates B_I^n as a function of the remote effective strain E_e^0 for different remote stress triaxialities R_σ and for various aspect ratios μ. It is clear at a glance from Fig. 5a that B_I^n increases monotonically with increasing the remote strain E_e^0 and with decreasing the stress triaxiality R_σ. This indicates that an increase in remote strain or a decrease in remote stress triaxiality elevates greatly the particle size effect on $K_I^{n\,max}$. In addition, Fig. 5b further shows that the elevation of B_I^n becomes more and more considerable with the particle shape ratio decreasing. In other words, the more oblate the particle is, the more significant the size effect on $K_I^{n\,max}$ is. This is easy to explain because larger interface curvature for more oblate particles can elevate strain gradient in the vicinity of particle equator and then aggravate the size effect.

Slipping and debonding of the particle/matrix interface also depend closely upon the shear SCF at the interface. Fig. 6 presents distributions of the interfacial shear SCF K_I^s along the interface for various particle
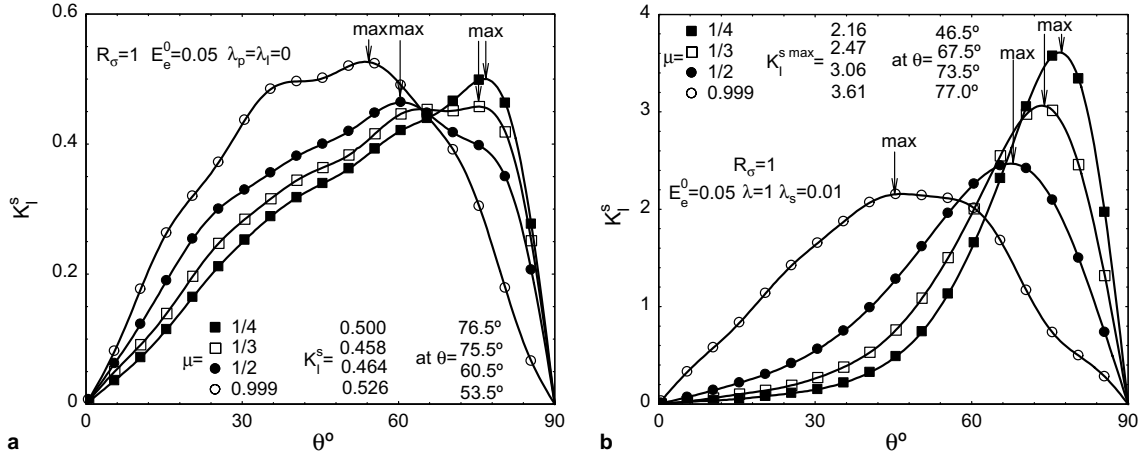
Fig. 6. Distribution of the interfacial shear SCF K_I^s along the particle surface for (a) scale-independent cases $\lambda_p = \lambda_I = 0$ and (b) scale-dependent cases $\lambda_p = 1, \lambda_I = 0.01$.

aspect ratios. For the size-independent cases (i.e. $\lambda_I = \lambda_p = 0$), Fig. 6a demonstrates clearly that the shear SCFs K_I^s are much less than 1 for both the spherical particle (treated as $\mu = 0.999$ approximately) and for the oblate ones $\mu < 1$. Hence, for the size-independent cases, the interface slip is relatively more difficult to occur. However, when the particle size falls into the micron or submicron range, the size effect arises as shown in Fig. 6b. Compared with the size-independent K_I^s at the interface, the size-dependent K_I^s is greatly elevated. This influence seems more and more significant with the particle aspect ratio decreasing. It suggests that the interface slip is much easier to initiate for the micron sized oblate particles.

To more closely examine the size effect on the interfacial shear SCF, normalizing the scale-dependent $\left(K_I^{s\,\max}\right)^{\lambda_p=1, \lambda_I=0.01}$ by the scale-independent $\left(K_I^{s\,\max}\right)^{\lambda_p=\lambda_I=0}$ can render a new parameter B_I^s. Similar with the ratio B_I^n, B_I^s increases gradually with increasing the remote effective strain E_e^0 and with decreasing the remote stress triaxiality R_σ or particle aspect ratio μ. Since the basic trends for B_I^n and B_I^s are similarly, the ratio B_I^n is not given schematically here.

4.3. Particle opening stress concentration factor K_p^o

Another possible void nucleation mechanism is the particle breakage, which is mainly governed by the opening stress $\sigma_{\theta\theta}$ on the particle equator plane ($\theta = 90°$ and $0 \leqslant \zeta \leqslant \beta$). Our results suggest that the opening stress on the particle equator plane is relatively uniform, so only the maximum opening SCF $K_p^{o\,\max}$ within the particle is schematically analyzed. Fig. 7 first plots size-independent variations of $\left(K_p^{o\,\max}\right)^{\lambda_p=\lambda_I=0}$ as the function of the remote effective strain for various particle shapes. From this figure, two interesting conclusions can be reached. One is that $K_p^{o\,\max}$ continually decreases with decreasing the particle aspect ratio. In other words, the opening SCF within the oblate particle is lower than that within the spherical particle for the same remote load condition. Another is that $K_p^{o\,\max}$ seems not very sensitive to the remote effective strain.

Fig. 8 shows variations of $B_p^o = \left(K_p^{o\,\max}\right)^{\lambda_p=1, \lambda_I=0.01} \Big/ \left(K_p^{o\,\max}\right)^{\lambda_p=\lambda_I=0}$ with the remote effective strain, which can illustrate the size effect on $K_p^{o\,\max}$ clearly. It can be seen that B_p^o is always larger than 1. This means that the size effect elevates the maximum opening SCF $K_p^{o\,\max}$ on the particle equator plane. Further, this eleva-
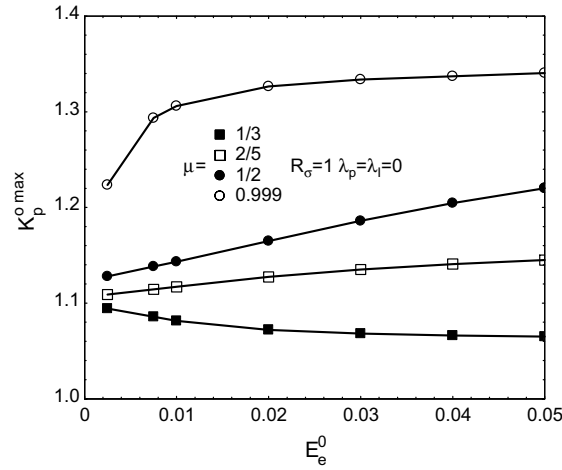
Fig. 7. Variations of the size-independent maximum particle opening SCF $\left(K_p^{o\,max}\right)^{\lambda=\lambda_s=0}$ with the remote effective strain E_e^0 for various particle aspect ratios $\mu = \left\{0.999, \frac{1}{2}, \frac{2}{5}, \frac{1}{3}\right\}$.
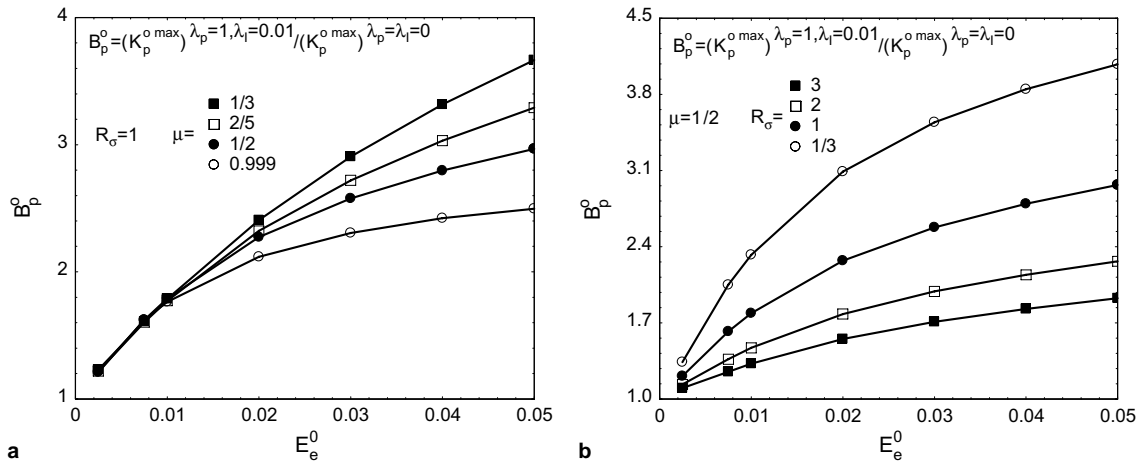

Fig. 8. Variations of the ratio $B_p^o = (K_p^{o\,max})^{\lambda_p=1,\lambda_I=0.01}/(K_p^{o\,max})^{\lambda_p=\lambda_I=0}$ with the remote effective strain (a) for different particles aspect ratios $\mu = \{0.999, \frac{1}{2}, \frac{2}{5}, \frac{1}{3}\}$ and (b) for various stress triaxialities $R_\sigma = \{1/3, 1, 2, 3\}$.

tion becomes more and more significant with increasing the remote strain (see Fig. 8a) and decreasing the particle aspect ratio (see Fig. 8a) or the remote stress triaxiality (see Fig. 8b).

4.4. Ratio of particle opening SCF to interfacial normal SCF

As well known, the maximums of particle opening SCF $K_p^{o\,max}$ and interfacial normal SCF $K_I^{n\,max}$ play important roles in the particle cracking and interface debonding void nucleation mechanisms, respectively. Fig. 9 displays influences of the size effect and the shape effect on the variations of the ratio $B_{pi} = K_p^{o\,max}/K_I^{n\,max}$ with the remote effective strains E_e^0. It can be found from this figure that, for the size-independent case (i.e. $\lambda = \lambda_s = 0$), B_{pi} are very close to 1.0 or even less than 1.0. This is basically consistent with some experiment observations that the voids are apt to initiate by particle/matrix interface debonding
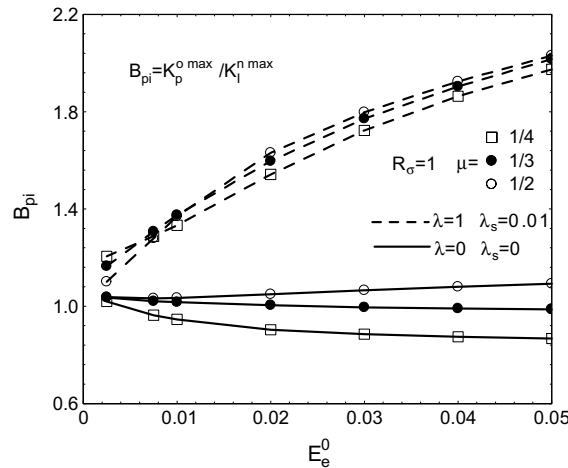
Fig. 9. A ratio $B_{pi} = K_p^{o\,max}/K_I^{n\,max}$ of the maximum opening SCF within the particle to the maximum normal SCF at the particle/matrix interface shown as a function of the remote effective strain E_e^0 for both the size-dependent and the size-independent cases.

for the oblate particle, especially when the particle aspect ratio is small. However, with the particle size decreasing and falling into the micron or even submicron size (e.g. $\lambda_p = 1$, $\lambda_I = 0.01$), B_{pi} becomes much larger than 1.0. This is completely different from the above size-independent cases. It means that if the critical strengths of the interfacial and particle are size-independent, the probability of the particle breakage nucleation mechanism would greatly increase for the micron sized oblate particle, especially at larger remote strain E_e^0. Of course, the strength of the particle is generally much stronger than that of the matrix/particle interface, so the void nucleation mechanism maybe still is governed by the interface separation. Further experimental studies on the critical particle and interface strengths in the micron or submicron range are very necessary to predict rationally the void nucleation mechanisms.

5. Summary

The main purpose of this paper is to study the coupled effects of particle size and shape on the stress concentrations and void nucleation mechanism. To achieve this end, an infinite power law SG solid with an oblate spheroidal particle under axis-symmetrical proportional and monotonic tension loading has been theoretically analyzed. Based on the three-function method in the classic elasticity, the deformation fields within the elastic oblate particle and in the non-linear matrix are given. To equilibrate the double-traction at the particle/matrix interface, an interface energy concept is especially introduced. By means of a Ritz method, the normal SCF K_I^n, the shear SCF K_I^s at the matrix–particle interface and the opening SCF K_p within the particle are numerically solved. Some interesting results are obtained as follows:

- The size effect significantly elevates the interfacial normal SCF K_I^n around the particle pole ($0° \leqslant \theta \leqslant 60°$) as well as the maximum $K_I^{n\,max}$. With the particle aspect ratio decreasing, the location of $K_I^{n\,max}$ shifts to the location with larger angle θ. Hence, the size effect is likely to advance the interface separation and change the location of void nucleation.
- The size-independent shear SCF K_I^s at the interface of the oblate particle is very small and the maximum $K_I^{s\,max}$ is usually less than 1. However, when the particle size effect comes into effect, the maximum $K_I^{s\,max}$ is significantly enhanced to 2–3. This means that the void nucleation at the micron sized oblate particles is likely to be triggered by the particle/matrix interface slip.

- The opening SCF within the particle is dramatically increased by the size effect and this elevation is much more significant than that of the interfacial normal SCF. Although the probability of particle breakage is likely to increase, whether particle cracking or interface debonding is the eventual void nucleation mechanism mainly rests with the critical strengths of the tiny particle and interface.
- The increases in the remote strain level and decreases in the remote stress triaxiality or in the particle aspect ratio can aggravate the size effects on the SCFs. This is not difficult to understand because the higher strain level and the larger interface curvature near particle equator can induce severer strain gradient.
- For the oblate particle, the influences of the interface energy on the interfacial SCFs especially on the normal interfacial SCF are very weak but much stronger on the opening SCF within in the particle; while for the prolate particles, the interfacial energy decreases the interfacial normal SCF to a certain extent but elevates the interfacial shear and particle opening SCFs.

It is worthy to note that the isotropic interfacial energy density is tentatively suggested as $w^I = G_m l_I u_{i,j} u_{i,j}$ for simplicity. Further studies on the form of the interfacial energy and the interfacial characteristic length l_I are also very valuable.

Acknowledgements

Appendix A

Referring to Lee and Mear (1999), the correlation between the Cartesian system (x_1, x_2, x_3) and the oblate spheroidal coordinates (ζ, θ, ψ) is

$$\begin{cases} x_1 = \alpha \cosh \zeta \sin \theta \cos \psi, \\ x_2 = \alpha \cosh \zeta \sin \theta \sin \psi, \\ x_3 = \alpha \sinh \zeta \cos \theta. \end{cases} \tag{A.1}$$

Let $\{e_1, e_2, e_3\}$ represent the unit base vectors for the Cartesian coordinate system and $\{e_\zeta, e_\theta, e_\psi\}$ for the oblate spheroidal coordinate system. According to the Boussinesq's relation (i.e. the three-function method, Gurtin, 1984), the axisymmetric displacement field within the elastic particle and in the elastic matrix can be given by

$$\boldsymbol{u} = \gamma \Psi e_3 - \nabla(x_3 \Psi + \Phi), \tag{A.2}$$

where $e_3 = \frac{\alpha}{h}(\cosh \zeta \cos \theta e_\zeta - \sinh \zeta \sin \theta e_\theta)$, $h = \alpha \sqrt{\cosh^2 \zeta - \sin^2 \theta}$, $\gamma = 4(1-v)$ and v is Poisson's ratio. The functions Ψ and Φ, which only depend upon $\{\zeta, \theta\}$, are harmonic, so

$$\nabla^2 \Psi = \nabla^2 \Phi = 0, \tag{A.3}$$

where ∇^2 and ∇ are the Laplacian and the gradient operator, respectively. In the present oblate spheroidal coordinate system, they can be written as

$$\nabla^2 = \frac{1}{h}\left(\frac{\partial^2}{\partial \zeta^2} + \tanh \zeta \frac{\partial}{\partial \zeta} + \frac{\partial^2}{\partial \theta^2} + \cot \theta \frac{\partial}{\partial \theta}\right) \tag{A.4}$$

and

$$\nabla = \frac{1}{h}\left(\frac{\partial}{\partial\zeta}\boldsymbol{e}_\zeta + \frac{\partial}{\partial\theta}\boldsymbol{e}_\theta\right). \tag{A.5}$$

It is easy to validate that following separable variable terms can meet automatically the oblate-spheroidal harmonic condition (A.3):

$$P_n(\mathrm{i}\sinh\zeta)P_n(\cos\theta) \quad\text{and}\quad Q_n(\mathrm{i}\sinh\zeta)P_n(\cos\theta), \tag{A.6}$$

where $\mathrm{i} = \sqrt{-1}$, P_n and Q_n are the Legendre polynomials and Legendre functions of the second kind, respectively. Therefore complete separable variable solutions for $\{\Psi, \Phi\}$ can be constructed as

$$\begin{cases} \Psi = -\sum_{n=0,1,2} \mathrm{i}^m\alpha(2n+1)E_nR_n(\mathrm{i}\sinh\zeta)P_n(\cos\theta), \\[2mm] \Phi = -\sum_{n=-1,0,1} \mathrm{i}^{m-1}\alpha^2 G_{n+1}R_{n+1}(\mathrm{i}\sinh\zeta)P_{n+1}(\cos\theta), \end{cases} \tag{A.7}$$

where E_n and G_n are free real constants,

$$R_n = \begin{cases} P_n(\mathrm{i}\sinh\zeta) & \text{for the inclusion,} \\ Q_n(\mathrm{i}\sinh\zeta) & \text{for the matrix} \end{cases} \quad\text{and}\quad m = \begin{cases} n+2 & \text{for the inclusion,} \\ n+1 & \text{for the matrix.} \end{cases}$$

Substituting (A.7) into (A.2), removing the redundant terms and noting that the displacement field is symmetry with respect to the median plane $\theta = \frac{\pi}{2}$, the elastic displacement field can be written as

$$\begin{cases} u_\zeta = -\dfrac{\mathrm{i}\alpha^2}{h}H_{-1}R_0^1 + \dfrac{\alpha^2}{h}\sum_{n=1,3,5,\ldots}\mathrm{i}^{m-1}\{[H_nR_{n+1}^1 + (n+1)(n+\gamma)I_nR_{n-1}^1]P_{n+1}(\cos\theta) \\ \qquad + n(n+1-\gamma)I_nR_{n+1}^1 P_{n-1}(\cos\theta)\}, \\[2mm] u_\theta = \dfrac{\alpha^2}{h}\sum_{n=1,3,5,\ldots}\mathrm{i}^{m-1}\{[H_nR_{n+1} + n(n+1-\gamma)I_nR_{n-1}]P_{n+1}(\cos\theta) \\ \qquad + (n+1)(n+\gamma)I_nR_{n+1}P_{n-1}(\cos\theta)\}, \end{cases} \tag{A.8}$$

where P_n^1 and are the one order associated Legendre functions of the first kind and the second kind, respectively. $\{H_n, I_n\}$ are real constants and R_n^1 is function of $\mathrm{i}\sinh\zeta$, which can be expressed as

$$\begin{cases} H_n = G_{n+1} + \dfrac{(n+1)(n+1-\gamma)}{2n+1}E_n, \\[2mm] I_n = \dfrac{E_n}{2n+1} \end{cases} \quad\text{and}\quad R_n^1 = \begin{cases} P_n^1(\mathrm{i}\sinh\zeta) & \text{for the inclusion,} \\ Q_n^1(\mathrm{i}\sinh\zeta) & \text{for the matrix.} \end{cases} \tag{A.9}$$

Appendix B

Following Lee and Mear (1999) to insure the displacement field is continuous across the matrix–particle interface, the displacement fields in the matrix and within the particle must satisfy

$$\boldsymbol{u}^p = \boldsymbol{U}^0 + \tilde{\boldsymbol{u}} \quad\text{on } \zeta = \beta. \tag{B.1}$$

Clearly, this equation establishes the correlations between the constants $\{H_j, I_j\}$ associated with the particle displacement field and the real coefficients involved in the trial reduced matrix displacement field. At the 'ζ-direction', the constraint conditions (B.1) can be expressed as

$$\begin{cases} i^2(2-\gamma^p)I_1P_2^1 = \dfrac{E_m^0}{3}P_2^1(\cosh\beta) + F_0(\beta) = \mathscr{A}_0, \\[2mm] i^4[3(4-\gamma^p)I_3] + i^2H_{n-1}P_n^1 = \dfrac{E_e^0}{3}P_2^1(\cosh\beta) + F_2(\beta) = \mathscr{A}_2, \\[2mm] i^k[H_{k-1}P_k^1 + k(k-1+\gamma^p)I_{k-1}P_{k-2}^1] + i^{k+2}[(k+1)(k+2-\gamma^p)I_{k+1}P_{k+2}^1] = F_k(\beta) = \mathscr{A}_k \quad k=4,6,8,\dots \end{cases}$$

(B.2)

At the 'θ-direction', the constraint conditions (B.1) can be written as

$$\begin{cases} i^2[H_1P_2 + (2-\gamma^p)I_1] + i^4[4(3+\gamma^p)I_3P_4] = \dfrac{E_e^0 - E_m^0}{3} + \dfrac{E_e^0 P_2(\sinh\beta)}{3} + G_2(\beta) = \mathscr{B}_2, \\[2mm] i^n[H_{k-1}P_k + (k-1)(k-\gamma^p)I_{k-1}P_{k-2}] + i^{k+2}[(k+2)(k+1+\gamma^p)I_{k+1}P_{k+2}] = G_k(\beta) = \mathscr{B}_k \quad k=4,6,8,\dots, \end{cases}$$

(B.3)

where the arguments of the functions P_k and are all isinh β, the new parameters $\mathscr{A}_k$ and $\mathscr{B}_k$ are the linear combinations of A_{km} and B_{km}, respectively.

By solving the equation groups (B.2) and (B.3), the constants $\{H_k, I_k\}$ can be readily expressed in terms of $\{\mathscr{A}_k, \mathscr{B}_k\}$ (i.e. in terms of $\{A_{km}, B_{km}\}$):

$$\begin{cases} I_1 = \dfrac{\alpha_0}{i^2(2-\gamma^p)P_2^1}, \\[3mm] I_{k+1} = \dfrac{1}{\Omega_{k+1}}[i^kP_k^1\mathscr{B}_k - i^kP_k\mathscr{A}_k - \Omega_{k-1}I_{k-1}], \qquad k=2,4,\dots, \\[3mm] H_{k-1} = \dfrac{i^{k+2}}{\Omega_{k+1}}[(k+2)(k+1+\gamma^p)P_{k+2}\mathscr{A}_k \\[2mm] \qquad\quad -(n+1)(n+2-\gamma^p)P_{k+2}^1\mathscr{B}_k] + \frac{\Lambda_k}{\Omega_{k+1}}I_{k-1}, \end{cases}$$

(B.4)

where

$$\begin{cases} \Omega_k = i^k[(k+2)(k+1+\gamma^p)P_{k-1}^1P_{k+1} - k(k+1-\gamma^p)P_{k-1}P_{k+1}^1], \\[2mm] \Lambda_k = i^{2k+2}[(k-1)(k-\gamma^p)(k+1)(k+2-\gamma^p)P_{k-2}P_{k+2}^1 \\[2mm] \qquad\quad -k(k+2)(k+1+\gamma^p)(k-1+\gamma^p)P_{k+2}P_{k-2}^1]. \end{cases}$$

(B.5)

Apparently, the independent unknown parameters in the displacement fields within the particle and in the matrix are $\{A_{km}, B_{km}\}$.

References

Abu Al-Rub, R.K., Voyiadjis, G.Z., 2004. Analytical and experimental determination of the material intrinsic length scale of strain gradient plasticity theory from micro- and nano-indentation experiments. Int. J. Plast. 20, 1139–1182.

Acharya, A., Bassani, J.L., 2000. Lattice incompatibility and a gradient theory of crystal plasticity. J. Mech. Phys. Solids 48, 1565–1595.

Aifantis, E.C., 1984. On the microstructural origin of certain inelastic models. Trans. ASME J. Eng. Mater. Tech. 106, 326–330.

Aifantis, E.C., 1987. The physics of plastic deformation. Int. J. Plast. 3, 211–247.

Aifantis, K.E., Willis, J.R., 2005. The role of interfaces in enhancing the yield strength of composites and polycrystals. J. Mech. Phys. Solids 53, 1047–1070.

Arzt, E., 1998. Size effects in materials due to microstructural and dimensional constraints: a comparative review. Acta Mater. 46, 5611–5626.

Barlow, C.Y., Liu, Y.L., 1998. Microstructure, strain fields and flow stress in deformed metal matrix composites. Acta Metall. Mater. 46, 5807.

Bassani, J.L., 2001. Incompatibility and a simple gradient theory of plasticity. J. Mech. Phys. Solids 49, 1983–1996.

Begley, M.R., Hutchinson, J.W., 1998. The mechanics of size-dependent indention. J. Mech. Phys. Solids 46, 2049–2068.

Bittencourt, E., Needleman, A., Gurtin, M.E., Van der Giessen, E., 2003. A comparison of nonlocal continuum and discrete dislocation plasticity predictions. J. Mech. Phys. Solids 51, 281–310.

Brechet, Y., Embury, J.D., Tao, S., Luo, L., 1991. Damage initiation in metal matrix composites. Acta Metall. Mater. 39, 1781–1786.

Budiansky, B., Hutchinson, J.W., Slutsky, S., 1982. Void growth and collapse in viscous solids, solid mechanics. In: Hopkins, H.G., Swell, M.J. (Eds.), The Rodney Hill 60th Anniversary Volume. Pergamon Press, Oxford, pp. 13–45.

Cermelli, P., Gurtin, M.E., 2002. Geometrically necessary dislocations in viscoplastic single crystals and bicrystals undergoing small deformations. Int. J. Solids Struct. 39, 6281–6309.

Cleveringa, H.H.M., Van der Giessen, E., Needleman, A., 1997. Comparison of discrete dislocation and continuum plasticity predictions for a composite material. Acta Mater. 45, 3163–3179.

Cleveringa, H.H.M., Van der Giessen, E., Needleman, A., 1999a. A discrete dislocation analysis of residual stress in a composite material. Philos. Mag. A 79, 863–920.

Cleveringa, H.H.M., Van der Giessen, E., Needleman, A., 1999b. A discrete dislocation analysis of bending. Int. J. Plast. 15, 837–868.

Deshpande, V., Needleman, A., Van der Giessen, E., 2003. Finite strain discrete dislocation plasticity. J. Mech. Phys. Solids 51, 2057–2083.

Espinosa, H.D., Prorok, B.C., Fisher, M., 2003. A methodology for determining mechanical properties of free standing thin films and mems materials. J. Mech. Phys. Solids 51, 47–67.

Espinosa, H.D., Prorok, B.C., Peng, B., 2004. Plasticity size effects in free-standing submicron polycrystalline FCC films subjected to pure tension. J. Mech. Phys. Solids 52, 667–689.

Fisher, J.R., Gurland, J., 1981. Void nucleation in spheroidized carbon steels part 1: experimental. Metal. Sci. 15, 185.

Fleck, N.A., Hutchinson, J.W., 1993. A phenomenological theory for strain gradient effects in plasticity. J. Mech. Phys. Solids 41, 1825–1857.

Fleck, N.A., Hutchinson, J.W., 1997. Strain gradient plasticity. In: Hutchinson, J.W., Wu, T.Y. (Eds.), Advance in Applied Mechanics, vol. 33. Academic Press, New York, pp. 295–361.

Fleck, N.A., Hutchinson, J.W., 2001. A reformulation of strain gradient plasticity. J. Mech. Phys. Solids 49, 2245–2271.

Fleck, N.A., Muller, G.M., Ashby, M.F., Hutchinson, J.W., 1994. Strain gradient plasticity: theory and experiment. Acta Mater. 42, 475–487.

Gao, H., Huang, Y., Nix, W.D., Hutchinson, J.W., 1999. Mechanism-based gradient plasticity—I. Theory. J. Mech. Phys. Solids 47, 1239–1263.

Gudmundson, G., 2004. A unified treatment of strain gradient plasticity. J. Mech. Phys. Solids 52, 1379–1406.

Gurtin, M.E., 1984. The linear theory of elasticity. In: Truesdell, C. (Ed.), Mechanics of Solids, vol. II. Springer-Verlag, New York, p. 1.

Gurtin, M.E., 2000. On the plasticity of single crystals: free energy, microforces, plastic-strain gradient. J. Mech. Phys. Solids 48, 989–1036.

Han, C.S., Gao, H., Huang, Y., Nix, W., 2005a. Mechanism-based strain gradient crystal plasticity—I. Theory. J. Mech. Phys. Solids 53, 1188–1203.

Han, C.S., Gao, H., Huang, Y., Nix, W., 2005b. Mechanism-based strain gradient crystal plasticity—II. Analysis. J. Mech. Phys. Solids 53, 1204–1222.

Hill, R., 1956. New horizons in the mechanics of solids. J. Mech. Phys. Solids 5, 66.

Huang, H., Spaepen, H., 2000. Tensile testing of free standing Cu, Ag and Al thin films and Ag/Cu multilayers. Acta Mater. 48, 3261–3269.

Huang, M.S., Li, Z.H., 2005. Size effects on stress concentration induced by a prolate ellipsoidal particle and void nucleation mechanism. Int. J. Plast. 21, 1568–1590.

Huang, W.C., 1972. Theoretical study of stress concentrations at circular hole and inclusion in strain-hardening materials. Int. J. Solids Struct. 8, 149.

Huang, Y., Gao, H., Nix, W.D., Hutchinson, J.W., 2000. Mechanism-based strain gradient plasticity II. Analysis. J. Mech. Phys. Solid 48, 99–128.

Hutchinson, J.W., 2000. Plasticity at micron scale. Int. J. Solids Struct. 37, 225–238.

Hwang, K.C., Huang, Y., 2002. The Constitutive Theory of Solid, the Strain Gradient Theory, second ed. Tsinghua University Press, Beijing (in Chinese).

Keer, L.M., Dundurs, J., Kiattikomol, K., 1973. Separation of a smooth circular particle from a matrix. Int. J. Eng. Sci. 11, 1221–1233.

Lee, B.J., Mear, M.E., 1999. Stress concentration induced by an elastic spheroidal particle in a plastically deforming solid. J. Mech. Phys. Solids 47, 1301–1336.

Lloyd, D.J., 1991. Aspects of fracture in particulate reinforced metal matrix composites. Acta Metall. Mater. 39, 59–71.

Lloyd, D.J., 1994. Particle reinforced aluminum and magnesium matrix composites. Int. Mater. Rev. 39, 1–23.

Ma, Q., Clark, D.R., 1995. Size dependent hardness in silver single crystals. J. Mater. Res. 10, 853–863.

Manoharan, M., Lewandowski, J.J., 1990. Crack initiation and growth toughness of an aluminum metal-matrix composite. Acta Metall. 38, 489–496.

McDanels, D.L., Serafini, T.T., Dicarlo, J.A., 1985. Polymer, metal, and ceramic matrix composites for advanced aircraft engine applications. NASA Technical Memorandum, 25p.

McElhaney, K.W., Vlassak, J.J., Nix, W.D., 1998. Determination of indenter tips geometry and indentation contact area for depth-sensing indentation experiments. J. Mater. Res. 13, 1300–1306.

Needleman, A., 1987. A continuum model for void nucleation by inclusion debonding. J. Appl. Mech. 54, 525–531.

Nicola, L., Van der Giessen, E., Needleman, A., 2003. Discrete dislocation analysis of size effects in thin films. J. Appl. Phys. 93, 5920–5928.

Niordson, C.F., 2003. Strain gradient plasticity effects in whisker-reinforced metals. J. Mech. Phys. Solids 51, 1863–1883.

Niordson, C.F., Tvergaard, V., 2001. Nonlocal plasticity effects on the tensile properties of a metal matrix composite. Eur. J. Mech. A/Solids 20, 601–613.

Niordson, C.F., Tvergaard, V., 2002. Nonlocal plasticity effects on fiber debonding in a whisker-reinforced metal. Eur. J. Mech. A/Solids 21, 239–248.

Orr, J., Brown, D.K., 1974. Elastio-plastic solutions for a cylindrical inclusion in plane strain. Eng. Fract. Mech. 6, 261.

Shi, M.X., Huang, Y., Gao, H., 2003. The *J*-integral and geometrically necessary dislocation in nonuniform plastic deformation. Int. J. Plast. 20, 1371–1386.

Shu, J.Y., Barlow, C.Y., 2000. Strain gradient effects on microscopic strain field in a metal matrix composite. Int. J. Plast. 16, 563–591.

Shu, J.Y., Fleck, N.A., Van der Giessen, E., Needleman, A., 2001. Boundary layers in constrained plastic flow: comparison of nonlocal and discrete dislocation plasticity. J. Mech. Phys. Solids 49, 1316–1395.

Smyshlyaev, V.P., Fleck, N.A, 1996. The role of strain gradients in the grain size effect for polycrystals. J. Mech. Phys. Solids 44, 465–496.

Stolken, J.S., Evans, A.G., 1998. A Microbend test method for measuring the plasticity length scale. Acta Mater. 46, 5109–5115.

Thomson, R.D., Hancock, J.W., 1984. Local stress and strain fields near a spherical near a spherical elastic particle in a plastically deforming matrix. Int. J. Fract. 24, 209.

Tuba, I.S., 1966. Elastic-plastic analysis of a flat plate with a circular rigid inclusion. Appl. Sci. Res. 16, 241.

Tvergaard, V., 1993. Model studies of fiber breakage and debonding in a metal reinforced by short fibers. J. Mech. Phys. Solids 41, 1309–1326.

Tvergaard, V., 1995. Fiber debonding and breakage in whisker-reinforced metal. Mater. Sci. Eng. A 190, 215–222.

Wilner, B., 1988. Stress analysis of particles in metals. J. Mech. Phys. Solids 36, 141–165.

Wilner, B., 1995. Asymptotic stress analysis of two phase materials. Int. J. Eng. Sci. 33, 127–130.

Xue, Z., Huang, Y., Li, M., 2002. Particle size effect in metallic materials: a study by the theory of mechanism-based strain gradient plasticity. Acta Mater. 50, 149–160.